

Ge doping of GaN beyond the Mott transition using Plasma-Assisted Molecular-Beam Epitaxy

A. Ajay^{1,2}, J. Schörmann³, M. Jiménez-Rodríguez^{1,2,4}, C. B. Lim^{1,2}, M. I. Den Hertog^{1,5},
F. Walther³, M. Rohnke⁶, M. Eickhoff³ and E. Monroy^{1,2}

¹ Université Grenoble-Alpes, 38000 Grenoble, France.

² CEA-Grenoble, INAC-PHELIQS, 17 av. des Martyrs, 38000 Grenoble, France.

³ I. Physikalisches Institut, Justus-Liebig-Universität Gießen and Center for Materials Science, Heinrich-Buff-Ring 16, 35392 Gießen, Germany.

⁴ GRIFO, Dept. Electrónica, Universidad de Alcalá, 28871 Alcalá de Henares, Madrid, Spain.

⁵ CNRS-Institute Néel, 25 av. des Martyrs, 38000 Grenoble, France.

⁶ Physikalisches-Chemisches Institut and Center for Materials Science, Justus-Liebig-Universität Gießen, Heinrich-Buff-Ring 17, 35392 Gießen, Germany

Abstract

We present a study of germanium as n-type dopant in wurtzite GaN films grown by plasma-assisted molecular beam epitaxy, reaching carrier concentrations of up to $6.7 \times 10^{20} \text{ cm}^{-3}$ at 300K, well beyond the Mott density. The Ge concentration and free carrier density were found to scale linearly with the Ge flux in the studied range. All the GaN:Ge samples present smooth surface morphology with atomic terraces, without trace of pits or cracks, and the mosaicity of the samples has no noticeable dependence on the Ge concentration. The variation of the GaN:Ge band gap with the carrier concentration is consistent with theoretical calculations of the band gap renormalization due to electron-electron and electron-ion interaction, and Burstein-Moss shift.

Keywords: Doping, Ge, GaN, thin films, MBE

Silicon has been the preferred n-type dopant for wurtzite GaN, even though it contributes to edge type dislocation climb, leading to an increase in tensile stress.¹⁻³ Tensile strain is especially troublesome when growing GaN on silicon substrates, where the mismatch of thermal expansion coefficients requires careful strain engineering to avoid cracking.⁴ Furthermore, doping with Si in excess of 10^{19} cm^{-3} , i.e. above the Mott transition in GaN, is reported to cause surface roughening and eventually crack propagation.² In nanowire structures, currently under investigation for a new generation of light emitting diodes, the radial distribution of Si is inhomogeneous, with a tendency to migrate towards the sidewalls,⁵ and high doping levels tend to degrade the nanowire morphology.⁶

In response, Ge was recently reintroduced as a highly favorable n-type dopant in GaN, with the possibility for higher doping concentrations.^{2,3} Ge, like Si, is a shallow donor in GaN, with a theoretical activation energy of 31.1 meV.⁷ The ionic radius of Ge atom is similar to that of Ga and the metal-nitrogen bond length changes by only 1.4% with Ge, compared to 5.5% with Si.⁸ Hence Ge can occupy the Ga lattice site causing far less lattice distortion than other dopants like Si and O. Also like Si, the DX- state of Ge is unstable and does not affect doping efficiency.⁸ From both perspectives, fundamental and applied, it is important to perform extensive studies on Ge as a dopant in GaN.

A few studies regarding Ge doping of GaN using hydride vapor phase epitaxy (HVPE)⁹ and metalorganic vapor phase epitaxy (MOVPE)¹⁰⁻¹³ exist, and recent results on Si(111) substrates show the absence of additional tensile stress.^{3,12} Using plasma-assisted molecular-beam epitaxy (PAMBE), nanowires doped with Ge were also demonstrated to achieve significant dopant levels and metallic conductivity.^{14,15} In GaN/AlN nanowire heterostructures, the introduction of Ge doping has led to the demonstration of screening

of the internal electric field,^{16,17} and to the observation of intersubband transitions.¹⁸ However, there is still a large void regarding the effect of Ge doping on the PAMBE growth kinetics and properties of planar GaN:Ge.

In this work we analyze the effect of Ge on the PAMBE growth kinetics of GaN, and we demonstrate that concentrations up to $6.7 \times 10^{20} \text{ cm}^{-3}$ (i.e. 1.5% atomic incorporation), well above the Mott transition, do not perturb the growth process, the layer morphology or its structural quality. The GaN:Ge photoluminescence (PL) and band gap evolution with the doping level are consistent with theoretical calculations of the band gap renormalization and Burstein-Moss shifts.

GaN thin films were grown by PAMBE at a substrate temperature of $T_s = 720^\circ\text{C}$ and with a growth rate of 0.5 ML/s ($\approx 450 \text{ nm/h}$). The growth process was monitored by reflection high energy electron diffraction (RHEED) and the growth temperature was verified by measurement of the Ga desorption time from the GaN(0001) surface.¹⁹

Non-intentionally doped (n.i.d.) Ga-face GaN is synthesized by PAMBE under slightly Ga-rich conditions, with a 2-ML-thick self-regulated Ga adlayer on the growing surface.²⁰ The Ga adlayer is known to be sensitive to the presence of dopants. Particularly, silicon does not introduce any perturbation in the Ga kinetics; whereas segregation of Mg inhibits the formation of the Ga adlayer.²¹⁻²³ To analyze the effect of Ge on the adatom kinetics, we have studied the Ga desorption during a growth interruption after the deposition of 7 nm Ge-doped GaN for various Ge fluxes. The value of the Ga flux is approximately $\approx 0.7 \text{ ML/s}$, chosen so that the 2 ML Ga adlayer is dynamically stable during the growth of n.i.d. GaN, and an increase of Ga flux by 7% leads to the accumulation of Ga on the growing surface. After each measurement of Ga desorption from GaN:Ge, we deposit 7 nm of n.i.d. GaN and

record the Ga desorption from the undoped surface as a reference. Figure 1 presents the RHEED intensity transient generated by the Ga desorption after the growth of n.i.d GaN and Ge-doped GaN for Ge cell temperatures $T_{Ge} = 800^{\circ}\text{C}$, 900°C , 950°C and 1000°C . The RHEED intensity transients remain unaltered with the presence of a Ge flux, i.e. Ge does not perturb the Ga kinetics on the GaN(0001) growth front.

Following this information, Ge-doped GaN thin films with a thickness of 675 nm were grown in the 2 ML Ga-adlayer regime on 1- μm -thick AlN-on-sapphire templates. The samples were doped with Ge, varying T_{Ge} from 720°C to 1000°C (see list of samples in Table I). After the growth, the surface morphology was analyzed by atomic force microscopy (AFM) with the results presented in Fig. 2. Regardless of the doping level, all the samples present monoatomic terraces and hexagonally-shaped hillocks characteristic of PAMBE-grown GaN, without observation of cracks or pits. The root-mean-square (rms) roughness measured in $5 \times 5 \mu\text{m}^2$ images is 0.9 ± 0.3 nm for all the samples. These results demonstrate that there is no significant effect of Ge on the surface morphology. The structural quality was further examined by high-resolution x-ray diffraction (HRXRD) using a PANalytical X'Pert PRO MRD system with a bounce Ge(220) monochromator and a 0.114° collimator in front of the device. From ω - 2θ scans of the (0002) GaN reflection, the strain of the c-lattice parameter of GaN was estimated to $\varepsilon_{zz} = 0.23 \pm 0.08\%$ independent of Ge doping. This tensile strain along c is the result of the compressive in-plane stress imposed by the AlN substrat, in good agreement with previous studies of the plastic relaxation of GaN on AlN when growing by PAMBE in the 2 ML Ga-adlayer regime.²⁴ The full width at half maximum (FWHM) of the ω -scan of the (0002) reflection of GaN:Ge is compared to the n.i.d reference sample in Table I. For all the layers, the FWHM remains 190 ± 110 arcsec without any systematic influence of the Ge incorporation.

Electrical characterization was carried out using Hall Effect measurements in Van der Pauw geometry. Results at 300 K are given in Table I. Free carrier concentrations of up to $n = 6.7 \times 10^{20} \text{ cm}^{-3}$ are obtained. As illustrated in Fig. 3(a), n scales exponentially with the Ge cell temperature, following $n \propto \exp(-E_{Ge}/k_B T_{Ge})$, where $E_{Ge} = 3.58 \text{ eV}$ is the thermal evaporation energy of Ge, and k_B is the Boltzmann constant. This result points to a Ge concentration of at least $6.7 \times 10^{20} \text{ cm}^{-3}$, which corresponds to a Ge mole fraction higher than 1.5% in the layer. When increasing n from $7.9 \times 10^{17} \text{ cm}^{-3}$ to $6.7 \times 10^{20} \text{ cm}^{-3}$, the resistivity at 300 K (also in Table I) decreases over two orders of magnitude, reaching a lowest value of $6.90 \times 10^{-4} \Omega\text{cm}$ (sample I).

For a further analysis of the incorporation of Ge, all the samples were analyzed using time-of-flight secondary ion mass spectroscopy (ToF-SIMS) using a TOF.SIMS 5 system (ION-TOF GmbH) equipped with a 25 keV Bi-cluster primary ion gun and a 2 keV Cs-sputter gun. The depth profile of GaN:Ge sample H and the n.i.d reference sample X are described in Figs. 3(c,d) in arbitrary units. A uniform Ge signal throughout the thickness of the GaN layers is found. Oxygen and trace amounts of Si and C, seen in all samples including the reference, have no specific dependence on T_{Ge} . The carrier concentration extracted from Hall Effect measurements at room temperature scales linearly with the Ge signal obtained from ToF-SIMS, as shown in Fig. 3(b), confirming that the variation in carrier concentration is due to Ge incorporation.

Figures 4(a) and (b) describe the variation of carrier concentration and resistivity with temperature in samples with doping levels up to the density of the Mott transition ($\sim 1-1.5 \times 10^{19} \text{ cm}^{-3}$ in GaN at room temperature)^{25,26}. The activation energies E_a extracted from Fig. 4(a) decrease from 19.5 meV for sample A, to 12.4 meV for sample B, and 9.7 meV for sample C, in accordance to the decrease in average distance between the

impurity atoms.²⁷ Thus, the effective activation energy can be described by $E_a = E_I - \beta n^{1/3}$, where E_I is the activation energy of a single isolated Ge impurity atom in GaN (theoretically estimated at $E_I = 31.1$ meV by Wang and Chen⁷), and β is a proportionality constant. The value of α determined by the empirical fit is $(1.6 \pm 0.3) \times 10^{-5}$ meVcm, close to the $\beta = (2.1 \pm 0.2) \times 10^{-5}$ meVcm reported for Si donors.²⁸

The PL emission characteristics were analyzed by excitation with a continuous-wave solid-state laser ($\lambda = 244$ nm), with an excitation power around 250 μ W focused on a spot size of 100 μ m. The emission was collected by a Jobin Yvon HR460 monochromator equipped with an ultraviolet-enhanced CCD camera. Spectra recorded at low temperature ($T = 5$ K) and room temperature are displayed in Fig. 5(a) and (b), respectively. The PL spectra at 5 K of n.i.d GaN (sample X) show near-band-edge excitonic emission around 3.515 eV, blueshifted with respect to the theoretical value (in the range of 3.470 eV in bulk GaN) due to the in-plane compressive strain induced by the AlN substrate. Regardless of the temperature, as the Ge concentration increases, for samples A to C, a redshift is noticed consistent with the band gap renormalization (BGR)²⁹ due to electron-electron and electron-ion interaction. Further increase of carrier concentration (samples D to I) causes a blueshift of the emission due to the Burstein-Moss effect (BME).³⁰ The emission spectra of samples D to I are systematically broadened with increase in carrier concentration. The shape correspond to the Kane density of states for the conduction band multiplied by the Fermi-Dirac distribution, similar to the description in ref. [31].

The evolution of the band gap at room temperature was studied by optical transmission in the range from 320 nm to 420 nm. Measurements were performed under normal incidence, exciting with a 450 W Xe-arc lamp coupled to a Gemini-180 double

monochromator. The band gap energy (E_G), determined from Tauc's plot as displayed in the inset of Fig. 6, is provided in Table I. Similar to the low-temperature PL emission, the value of E_G first redshifts (samples A to C) and then blueshifts (samples D to I) with increasing carrier concentration, as illustrated in Fig. 6. In addition to the spectral shift, the increase in doping concentration also affects the sharpness of the absorption edge that can be described by introduction of an Urbach energy ΔE_{Urb} in the expression for the optical absorption: $\alpha(\lambda) = \alpha_0 \exp[(hc/\lambda - E_0)/\Delta E_{Urb}]$, where hc/λ is the photon energy, α_0 and E_0 are material-dependent fitting parameters. The values of ΔE_{Urb} extracted from transmission measurements are summarized in Table I, showing a monotonous increase with the carrier concentration.

The shift of the fundamental band gap with the free carrier concentration is given by the superposition of BGR and BME, i.e. $\Delta E = \Delta E_{BMS} + \Delta E_{BGR}$. We estimate individual contributions analytically similar to ref. [32]. The BGR shift itself has two contributions due to electron-electron and electron-ion interactions (ΔE_{ee} and ΔE_{ei} , respectively), which can be approximated as

$$\Delta E_{ee} = -\frac{e^2 k_F}{2\pi^2 \varepsilon_s \varepsilon_0} - \frac{e^2 k_{TF}}{8\pi \varepsilon_s \varepsilon_0} \left[1 - \frac{4}{\pi} \arctan\left(\frac{k_F}{k_{TF}}\right) \right]$$

$$\Delta E_{ei} = -\frac{e^2 n}{\varepsilon_s \varepsilon_0 a_{B^-}^* k_{TF}^3}$$

where e is the elementary charge, ε_0 is the vacuum permittivity, $\varepsilon_s = 9.38$ is the static dielectric constant of GaN, $k_F = (3\pi n)^{1/3}$ is the Fermi vector, $k_{TF} = 2\sqrt{k_F/(\pi a_{B^-}^*)}$ is the inverse Thomas-Fermi screening length, and $a_{B^-}^* = 4\pi \varepsilon_s \varepsilon_0 \hbar^2 / (m_e^* e^2)$ is the effective Bohr radius of the electron, with \hbar being the reduced Planck constant, and $m_e^* = 0.231m_0$ being the electron effective mass in GaN.

On the other hand, the shift induced by the BME follows the equation

$$\Delta E_{BMS} = \frac{\hbar^2 k_F^2}{2\mu^*}$$

where μ^* is the reduced effective mass.

The contribution from excitonic effects, influenced by carrier concentration, is weak at high carrier densities and is hence neglected here. A plot of ΔE is displayed in Fig. 6, showing good agreement with the band gap values obtained from Tauc's plot.

In conclusion, the effect of Ge doping in wurtzite GaN grown by PAMBE has been studied systematically. It was verified that the presence of a Ge flux does not perturb the Ga kinetics during the growth of GaN, even for $T_{Ge} = 1000^\circ\text{C}$. We have synthesized GaN:Ge with free carrier concentrations in the range of $7.9 \times 10^{17} \text{ cm}^{-3}$ to $6.7 \times 10^{20} \text{ cm}^{-3}$. We observed that the free carrier concentration scales linearly with the Ge incorporation. Regardless of the Ge concentration, all samples kept indistinguishable surface morphology with atomic terraces and a roughness in the $0.9 \pm 0.3 \text{ nm}$ range. The FWHM of the x-ray rocking curve in the $190 \pm 110 \text{ arcsec}$ range does not show any trend as a function of the doping level, showing that the mosaicity of the samples has no noticeable dependence on Ge doping in the range under study. Optical studies demonstrate variations of the GaN:Ge band gap consistent with theoretical calculations of the band gap renormalization due to electron-electron and electron-ion interaction and Burstein-Moss shift. In view of these results, the use of Ge appears as a satisfactory alternative to Si for n-type doping of GaN grown by PAMBE, particularly above the Mott density, where structural defects appear associated to Si incorporation.

Acknowledgements. Thanks are due to D. Boilot, Y. Genuist and Y. Curé for technical support, and to B. Gayral for fruitful discussions. The AlN-on-sapphire substrates were

supplied by DOWA Electronics Materials Co. Ltd. This work is supported by the EU ERC-StG “TeraGaN” (#278428) project, and by the French National Research Agency via the GaNEX program (ANR-11-LABX-0014).

References

- ¹ L.T. Romano, C.G. Van de Walle, J.W. Ager, W. Götz, and R.S. Kern, *J. Appl. Phys.* **87**, 7745 (2000).
- ² S. Fritze, A. Dadgar, H. Witte, M. Bügler, A. Rohrbeck, J. Bläsing, A. Hoffmann, and A. Krost, *Appl. Phys. Lett.* **100**, 122104 (2012).
- ³ C. Nenstiel, M. Bügler, G. Callsen, F. Nippert, T. Kure, S. Fritze, A. Dadgar, H. Witte, J. Bläsing, A. Krost, and A. Hoffmann, *Phys. Status Solidi RRL - Rapid Res. Lett.* **9**, 716 (2015).
- ⁴ A. Dadgar, S. Fritze, O. Schulz, J. Hennig, J. Bläsing, H. Witte, A. Diez, U. Heinle, M. Kunze, I. Daumiller, K. Haberland, and A. Krost, *J. Cryst. Growth* **370**, 278 (2013).
- ⁵ Z. Fang, E. Robin, E. Rozas-Jiménez, A. Cros, F. Donatini, N. Mollard, J. Pernot, and B. Daudin, *Nano Lett.* **15**, 6794 (2015).
- ⁶ T. Richter, H.L.R. Meijers, R. Calarco, and M. Marso, *Nano Lett.* **8**, 3056 (2008).
- ⁷ H. Wang and A.-B. Chen, *J. Appl. Phys.* **87**, 7859 (2000).
- ⁸ P. Bogusławski and J. Bernholc, *Phys. Rev. B* **56**, 9496 (1997).
- ⁹ Y. Oshima, T. Yoshida, K. Watanabe, and T. Mishima, *J. Cryst. Growth* **312**, 3569 (2010).
- ¹⁰ S. Nakamura, T. Mukai, and M. Senoh, *Jpn. J. Appl. Phys.* **31**, 2883 (1992).
- ¹¹ X. Zhang, P. Kung, A. Saxler, D. Walker, T.C. Wang, and M. Razeghi, *Appl. Phys. Lett.* **67**, 1745 (1995).
- ¹² A. Dadgar, J. Bläsing, A. Diez, and A. Krost, *Appl. Phys. Express* **4**, 011001 (2011).
- ¹³ R. Kirste, M.P. Hoffmann, E. Sachet, M. Bobea, Z. Bryan, I. Bryan, C. Nenstiel, A. Hoffmann, J.-P. Maria, R. Collazo, and Z. Sitar, *Appl. Phys. Lett.* **103**, 242107 (2013).
- ¹⁴ M. Schäfer, M. Günther, C. Länger, J. Müßener, M. Feneberg, P. Uredat, M.T. Elm, P. Hille, J. Schörmann, J. Teubert, T. Henning, P.J. Klar, and M. Eickhoff, *Nanotechnology* **26**, 135704 (2015).
- ¹⁵ J. Schörmann, P. Hille, M. Schäfer, J. Müßener, P. Becker, P.J. Klar, M. Kleine-Boymann, M. Rohnke, M. de la Mata, J. Arbiol, D.M. Hofmann, J. Teubert, and M. Eickhoff, *J. Appl. Phys.* **114**, 103505 (2013).
- ¹⁶ P. Hille, J. Müßener, P. Becker, M. de la Mata, N. Rosemann, C. Magén, J. Arbiol, J. Teubert, S. Chatterjee, J. Schörmann, and M. Eickhoff, *Appl. Phys. Lett.* **104**, 102104 (2014).
- ¹⁷ M. Beeler, C.B. Lim, P. Hille, J. Bleuse, J. Schörmann, M. de la Mata, J. Arbiol, M. Eickhoff, and E. Monroy, *Phys. Rev. B* **91**, 205440 (2015).
- ¹⁸ M. Beeler, P. Hille, J. Schörmann, J. Teubert, M. de la Mata, J. Arbiol, M. Eickhoff, and E. Monroy, *Nano Lett.* **14**, 1665 (2014).
- ¹⁹ P.K. Kandaswamy, F. Guillot, E. Bellet-Amalric, E. Monroy, L. Nevou, M. Tchernycheva, A. Michon, F.H. Julien, E. Baumann, F.R. Giorgetta, D. Hofstetter, T. Remmele, M. Albrecht, S. Birner, and L.S. Dang, *J. Appl. Phys.* **104**, 093501 (2008).
- ²⁰ C. Adelman, J. Brault, G. Mula, B. Daudin, L. Lymperakis, and J. Neugebauer, *Phys. Rev. B* **67**, 165419 (2003).
- ²¹ L. Lahourcade, J. Pernot, A. Wirthmüller, M.P. Chauvat, P. Ruterana, A. Laufer, M. Eickhoff, and E. Monroy, *Appl. Phys. Lett.* **95**, 171908 (2009).
- ²² E. Monroy, T. Andreev, P. Holliger, E. Bellet-Amalric, T. Shibata, M. Tanaka, and B. Daudin, *Appl. Phys. Lett.* **84**, 2554 (2004).
- ²³ J.E. Northrup, *Appl. Phys. Lett.* **86**, 122108 (2005).
- ²⁴ E. Bellet-Amalric, C. Adelman, E. Sarigiannidou, J.L. Rouvière, G. Feuillet, E. Monroy, and B. Daudin, *J. Appl. Phys.* **95**, 1127 (2004).
- ²⁵ F. Binet, J.Y. Duboz, J. Off, and F. Scholz, *Phys. Rev. B* **60**, 4715 (1999).
- ²⁶ M. Feneberg, K. Lange, C. Lidig, M. Wieneke, H. Witte, J. Bläsing, A. Dadgar, A. Krost, and R. Goldhahn, *Appl. Phys. Lett.* **103**, 232104 (2013).

- ²⁷ G.L. Pearson and J. Bardeen, Phys. Rev. **75**, 865 (1949).
- ²⁸ B.K. Meyer, D. Volm, A. Graber, H.C. Alt, T. Detchprohm, A. Amano, and I. Akasaki, Solid State Commun. **95**, 597 (1995).
- ²⁹ K.-F. Berggren and B.E. Sernelius, Phys. Rev. B **24**, 1971 (1981).
- ³⁰ T.S. Moss, Proc. Phys. Soc. B **67**, 775 (1954).
- ³¹ B. Arnaudov, T. Paskova, E.M. Goldys, S. Evtimova, and B. Monemar, Phys. Rev. B **64**, 045213 (2001).
- ³² M. Feneberg, S. Osterburg, K. Lange, C. Lidig, B. Garke, R. Goldhahn, E. Richter, C. Netzel, M.D. Neumann, N. Esser, S. Fritze, H. Witte, J. Bläsing, A. Dadgar, and A. Krost, Phys. Rev. B **90**, (2014).

Tables

Table I. Various parameters of the samples under study: Ge cell temperature (T_{Ge}), FWHM of the x-ray rocking curve ($\Delta\Omega$), room-temperature carrier concentration (n) and resistivity (ρ), band gap (E_G) and Urbach's tail energy (E_{Urb}) extracted from transmission measurements at room temperature.

Sample	T_{Ge} (°C)	$\Delta\Omega$ (arcsec)	n (cm ⁻³)	ρ (Ω cm)	E_G at 300 K (eV)	E_{Urb} at 300 K (meV)
A	720	133	7.89×10^{17}	8.1×10^{-2}	3.432	52.2
B	760	392	1.06×10^{18}	1.71×10^{-1}	3.436	53.3
C	800	120	2.45×10^{18}	2.61×10^{-2}	3.42	58.9
D	850	60	1.38×10^{19}	6.03×10^{-3}	3.43	66.0
E	875	100	3.13×10^{19}	3.27×10^{-3}	3.438	72.4
F	900	287	6.89×10^{19}	6.00×10^{-3}	3.484	94.9
G	925	115	1.55×10^{20}	8.75×10^{-4}	3.522	117
H	950	296	2.62×10^{20}	5.51×10^{-4}	3.58	132
I	1000	193	6.71×10^{20}	6.90×10^{-4}	3.671	198
X	n.i.d.	237	--	--	3.443	46.9

Figure captions

Figure 1: RHEED intensity oscillations during the Ga desorption after the growth of n.i.d. GaN and GaN:Ge growth at Ge cell temperatures $T_{Ge} = 800^{\circ}\text{C}$, 900°C , 950°C and 1000°C

Figure 2: AFM images of samples X, F and I. (Top: $1 \times 1 \mu\text{m}^2$ surface: z range 0–5 nm. Down: $2 \times 2 \mu\text{m}^2$ surface: z range 0–9 nm)

Figure 3: (a) Evolution of carrier concentration with the Ge cell temperature. (b) Comparison of carrier concentration and Ge ToF-SIMS signal showing a linear relationship. (c) ToF-SIMS profiles of GaN:Ge sample H, and (d) n.i.d GaN sample X.

Figure 4: Variation of (a) free carrier concentration and (b) resistivity with temperature for various GaN:Ge samples. Dashed lines in (a) correspond to exponential fits leading to the activation energy (E_a) values indicated in the figure. Inset: Variation of E_a as a function of the carrier concentration. The solid line is a fit to $E_a = E_I - \beta n^{1/3}$.

Figure 5: Photoluminescence spectra of various samples at (a) 5K and (b) 300K. The spectra are normalized and vertically shifted for clarity.

Figure 6: Variation of the band gap energy obtained from Tauc's plot as a function of the carrier concentration. The dashed line corresponds to the calculation of ΔE_{BGR} shifted by the band gap energy of the n.i.d sample X, and the solid line corresponds to the calculation of $\Delta E_{BGR} + \Delta E_{BME}$ shifted by the band gap of sample X. Inset: Tauc's plot of selected samples.

Figure 1

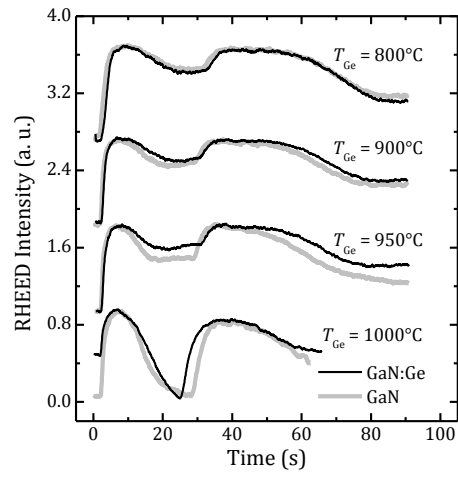


Figure 2

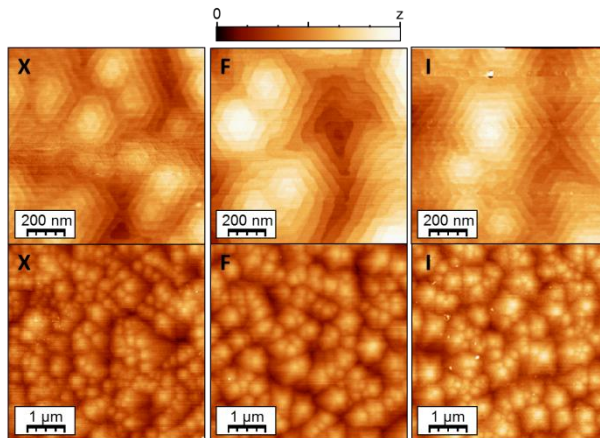


Figure 3

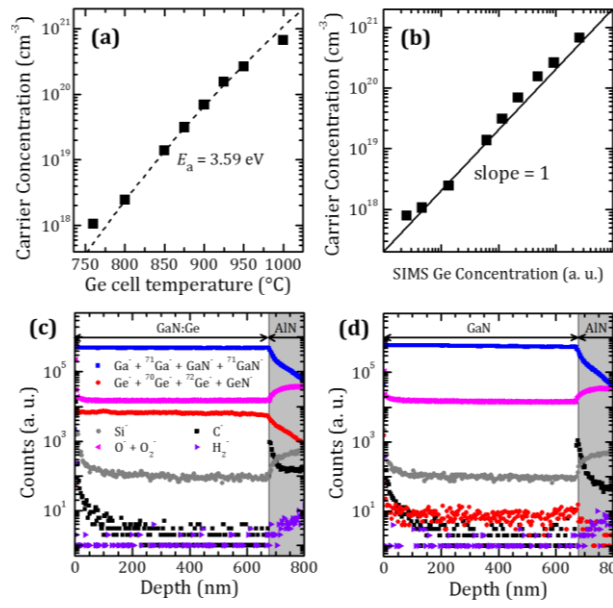


Figure 4

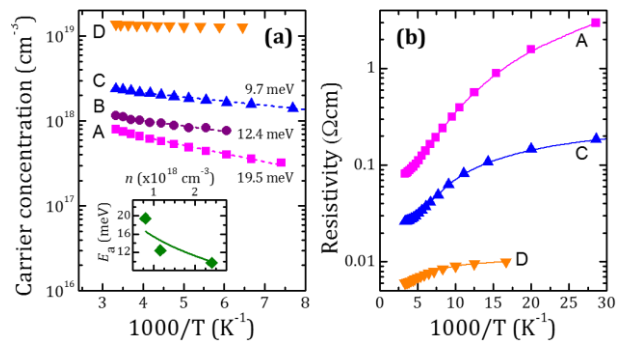


Figure 5

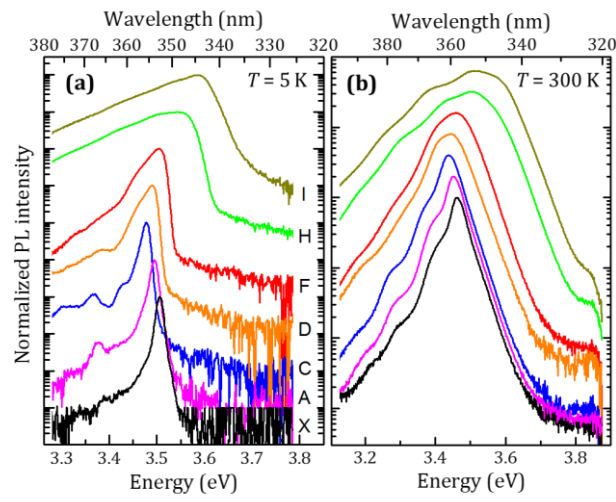


Figure 6

